



Two-dimensional Pd-nanosheets as efficient electrocatalysts for ethanol electrooxidation. Evidences of the C–C scission at low potentials

Majid Farsadrooh^{a,b}, Jorge Torrero^a, Laura Pascual^c, Miguel A. Peña^a, María Retuerto^a, Sergio Rojas^{a,*}

^a Grupo de Energía y Química Sostenible, ICP/CSIC, C/Marie Curie 2, 28049, Madrid, Spain

^b Department of Applied Chemistry, University of Sistan and Baluchestan, P.O. Box 98135 674, Zahedan, Iran

^c Instituto de Catálisis y Petroleoquímica, CSIC, C/Marie Curie 2, 28049, Madrid, Spain

ARTICLE INFO

Keywords:

Pd-nanosheets
EOR
Ethanol electrooxidation
Electrocatalysis
IRRAS
DEFC

ABSTRACT

Pd-nanosheets with a lateral size of ca. 5 nm have been prepared by a simple chemical method. The Pd-nanosheets obtained exhibited a 2D morphology in which Pd atoms are preferentially exposed at the surface of the particles. In addition, a preferential exposure of Pd atoms in 111 planes is observed. As a result, the Pd-nanosheets exhibit a very high catalytic activity for the electrooxidation of ethanol in alkaline electrolyte, superior to that of commercial nanosized Pd particles. In situ infrared studies conducted during the electrooxidation of ethanol reveal that the scission of the C–C bond of ethanol takes place at the surface of Pd-nanosheets at low potentials (as low as 30 mV). However, at higher potentials, the formation of partially oxidized species, typically acetates, is the preferred reaction pathway.

1. Introduction

The renewed interest in the study of the electrooxidation of ethanol accounts to its role in the renewable energy scenario [1–7]. Ethanol is a non-toxic, second generation liquid biofuel with higher theoretical mass energy density than methanol (8.01 vs 6.09 kW h kg^{−1}) [8]. It can be easily handled and storage thus being the ideal fuel for low temperature proton exchange membrane fuel cells. In direct ethanol fuel cells (DEFCs), aqueous solutions of ethanol are oxidized in the anode releasing electrons (and protons). The number of exchanged electrons per ethanol molecule ranges between 2 and 12, the most typical values being 2, 4, and 12 e[−] corresponding to the production of acetaldehyde, acetic acid, and CO₂, respectively. Even with the state-of-the-art Pt-based catalyst, partially oxidized C₂ molecules are the main reaction products [9,10]. The C₁ pathway, i.e., the scission of the C–C bond results in the formation CO₂ but also of strongly adsorbed intermediate species such as CO_{ads} and CH_{x,ads}, which are known to poison Pt-catalysts [11,12]. Such poisoning can be prevented by alloying Pt with oxophilic metals (Ru, Sn, Ir...) so that the nucleation of OH_{ads}, and thus CO_{ads} oxidation, is shifted to less positive potentials [9,13–15].

The recent development of anion exchange membranes paves the way for conducting ethanol electrooxidation in alkaline electrolyte [16]. It is widely accepted that electrooxidation reactions have faster kinetics in alkaline electrolytes than in acid ones [17]. Within this

context, Pd-based catalysts are attracting a great deal of attention as alternative catalysts for the electrooxidation of ethanol in alkaline media, and consequently numerous studies using Pd as anode electrode in DEFC have been published recently [18–24]. Thus, Ma. et al reported that Pd/C is more active than Pt/C for the EOR in alkaline electrolyte [25]. However, it should be acknowledged that similarly to Pt, Pd also occurs at extremely low levels in Earth's crust, so it is crucial to optimize Pd performance for the ethanol electrooxidation reaction (EOR).

Studies of the EOR with Pd are scarcer than with Pt. Most studies have been conducted with Pd black or Pd/C, and suggest that the EOR in alkaline electrolyte follows a similar reaction pathway than in acid one, yielding acetates along with a minor fraction of CO₂ (as carbonates) [25–28]. In addition, improvements of the catalytic activity of Pd can be achieved by properly tuning particle size and shape [29–32]. Thus, Pd nanocrystals in different shapes including nanospheres [33], concave nanocubes [34,35], nanowires [36], nanotubes [37], and nanosheets [38–40] have been synthesized. However, to our knowledge the effect of Pd morphology for the EOR in alkaline electrolyte has not been explored.

In this work we report a facile one pot synthesis of 2D palladium nanosheets by a simple chemical approach. Characterization results reveal the formation of 2D-like nanosheets resulting in a high fraction of surface Pd atoms. In addition, a preferential exposure of 111 planes is observed. As a result, this catalyst exhibits a superior performance

* Corresponding author.

E-mail address: srojas@icp.csic.es (S. Rojas).

<https://doi.org/10.1016/j.apcatb.2018.06.051>

Received 9 April 2018; Received in revised form 14 June 2018; Accepted 19 June 2018
Available online 20 June 2018

0926-3373/ © 2018 Elsevier B.V. All rights reserved.

towards the ethanol electrooxidation than that of nanosized spherical Pd particles. *in situ* infrared studies during the EOR reveal the scission of the C–C bond on Pd-nanosheets takes place at low potentials, but acetates are the majority product at high potentials.

2. Experimental

2.1. Materials

Palladium(II) acetylacetonate, acetic acid, potassium hydroxide, cetyltrimethylammonium bromide (CTAB), trioctylphosphine oxide (TOPO), chitosan ([2-amino-2-deoxy-(1–4)-b-D-glucopyranose]), (CH), Nafion 117 solution (~5% in a mixture of lower aliphatic alcohols and water) (N) which were purchased from Sigma–Aldrich without further purification and formic acid. Commercial Pd/C (10 wt% on activated carbon), commercial Pt/C (40 wt% on activated carbon). Ultrapure water (18.2 MV cm) produced through a Milli-Q system which was used in all aqueous solutions preparation and electrodes washing.

2.2. Synthesis of Pd nanosheets

In a typical synthesis, 10 mg of Pd (II) acetylacetonate, $\text{Pd}(\text{acac})_2$, was dissolved in 7 mL formic acid in a 15 mL glass vial. Then 170 mg of TOPO and 10 mg of CTAB were added to the solution and stirred for 30 min. The mixture was heated at 30 °C in a water bath for 20 min. The mixture was thoroughly degassed by bubbling N_2 and saturated with carbon monoxide at atmospheric pressure by bubbling CO during 10 min before the glass vial was capped, sealed with parafilm and aged in the water bath for 24 h. CO bubbling was conducted in a well-ventilated hood with external evacuation for CO. The $\text{Pd}(\text{acac})_2$ solutions were sealed with parafilm after CO bubbling in order to ensure a slow reduction of Pd(II) by CO which induces the formation of black particles. The solid was recovered and washed three times in acetone and ethanol under sonication.

2.3. Physicochemical characterization

Scanning Electron Microscopy (SEM) images were obtained in a JEOL JSM 7600F scanning electron microscope (SEM) operating at an accelerating voltage of 15 kV. Transmission Electron Microscopy (TEM) images of the as-prepared products were obtained in a JEM-2100F (JEOL) transmission electron microscope, operating at an accelerating voltage of 200 kV. High Angular Annular Dark Field–Scanning Transmission Electron Microscopy (HAADF-STEM) images were obtained operating at a camera length of 8 cm. Specimens for TEM analyses were prepared by sonicating the as-prepared catalyst powders in ethanol and adding a drop on 200 mesh TEM copper grid coated with a lacey carbon support film and dried in air. For the scanning electron microscopy studies a dispersion of the specimens under study in alcohol was deposited onto graphite sample holders and dried in air.

Information about the crystallographic structure and the purity of the as-prepared sample was determined by X-ray Powder Diffraction (XRD) in Bragg–Brentano reflection geometry with $\text{CuK}\alpha$ radiation ($\lambda = 1.5418 \text{ \AA}$). For the refinement of the crystal structure we used the Rietveld method and the Fullprof crystallographic program [41,42].

2.4. Electrochemical measurements

Electrochemical data were obtained using a computer controlled Autolab PGstat 302 N potentiostat/galvanostat. Experiments were recorded using a standard three-electrode cell at ambient temperature (about 25 °C). A gold wire and a silver/silver chloride electrode (Ag/AgCl) were used as counter and reference electrodes, respectively. N_2 -saturated 0.1 M KOH or 0.1 M KOH + 0.5 M $\text{CH}_3\text{CH}_2\text{OH}$ electrolytes were used. Unless otherwise stated, cyclic voltammograms were recorded at 10 mV s^{-1} between selected potentials. The electrocatalyst

under study were deposited on a 6 mm diameter glassy carbon electrode by means of an ink. Before the experiments, the glassy carbon electrode was polished with a $0.05 \mu\text{m}$ alumina slurry to a mirror-like surface, washed in acetone, ethanol and triply distilled water under ultra-sonication for 15 min.

First, a 2 mg/mL solution of chitosan (CH) into 1% acetic acid was prepared. Due to the low solubility of chitosan, the mixture was stirred thoroughly until a perfect solution was obtained. The solution was storage at 5 °C for 24 h and before use. 3 mg of the sample under study was added to a solution containing 2 mL of the chitosan-containing solution and 2 mL of ethanol and sonicated for 10 min to form a homogeneous mixture. Next, 15 μL of Nafion were added and sonicated for 10 min. 20 μL of the ink obtained were dropped on the GC electrode and dried under Ar flow. A thin layer of the electrocatalyst was formed containing 0.015 mg of catalyst.

The *in situ* FTIR (single potential alteration IR spectroscopy (SPAIRS)) experiments were collected using a NICOLET 6700 FT-IR spectrometer equipped inter-faced with the GPES software and with a He/Ne laser gun and liquid Nitrogen cooled MCT (mercury cadmium telluride) detector. The measurements were carried out in a three electrode home-made spectroelectrochemical cell (poly(methyl methacrylate)) (PMMA) equipped with a CaF_2 prism window, which is transparent to the incident beam in the spectral region ($1000\text{--}4000 \text{ cm}^{-1}$) on the bottom and connected to a potentiostat/galvanostat Autolab (PGstat 302 N). A gold wire electrode and a reversible hydrogen electrode (RHE) were used as counter and reference electrodes, respectively. The working electrode consisted of a gold disk of 10 mm diameter that was polished using alumina slurry prior to each measurement, washed with ultrapure water and dried under room temperature.

FTIR spectra were recorded between 4000 and 1100 cm^{-1} region with a resolution of 4 cm^{-1} . For the collection of the spectra, 0.5 M ethanol was added to the electrolyte, either KOH in H_2O or KOD in D_2O , and purged with N_2 at least 30 min. Then, the working electrode was pressed against the prism and, unless otherwise stated, a reference spectrum (R_0) was collected at a constant potential of 250 mV. Once the reference spectrum is stable, a process that usually takes more than 60 min, IR spectra were recorded between 0.25 and 1.2 V at a scan rate of 1 mV s^{-1} . Each spectrum was taken by accumulating 64 interferograms. IR spectra during EOR are reported as the R/R_0 ratio, in which R and R_0 are the spectra recorded at the selected and reference potentials, respectively. According to this description, negative going (downwards) bands indicated species being generated or an increase in their concentration with respect to the R_0 spectrum. Conversely, positive going (upward) bands corresponded to a decrease in concentration of the species.

3. Results

3.1. Materials characterization

Fig. 1 shows the x-ray diffractograms of the 2D Pd-nanosheets obtained. For comparison, the diffractogram of commercial Pd nanoparticles (Pd-black) is also shown. As observed, the diffractograms for both samples display the expected reflections for metallic Pd with fcc structure (space group $Fm\bar{3}m$). Mean domain crystallite sizes were estimated by applying the Scherrer equation to all diffraction lines, being $\sim 4 \text{ nm}$ for Pd-nanosheets and $\sim 9 \text{ nm}$ for Pd-black. Due to the unique morphology of the Pd particles in Pd-nanosheets exhibiting a 2D-growth (see below), particle size as determined from the reflections of a particular set of planes can be affected by lattice strain, *i.e.*, the crystallite size seems to decrease with the reflections at higher 2 θ values. By Rietveld refinement we obtained a cell parameter for Pd-nanosheets is $3.9136(4) \text{ \AA}$ and $V = 59.942(11) \text{ \AA}^3$ (see Fig. 1d)

The Rietveld refinement of the XRD data of the Pd-nanosheets confirms the preferential growth of the Pd-nanosheets exposing the 111

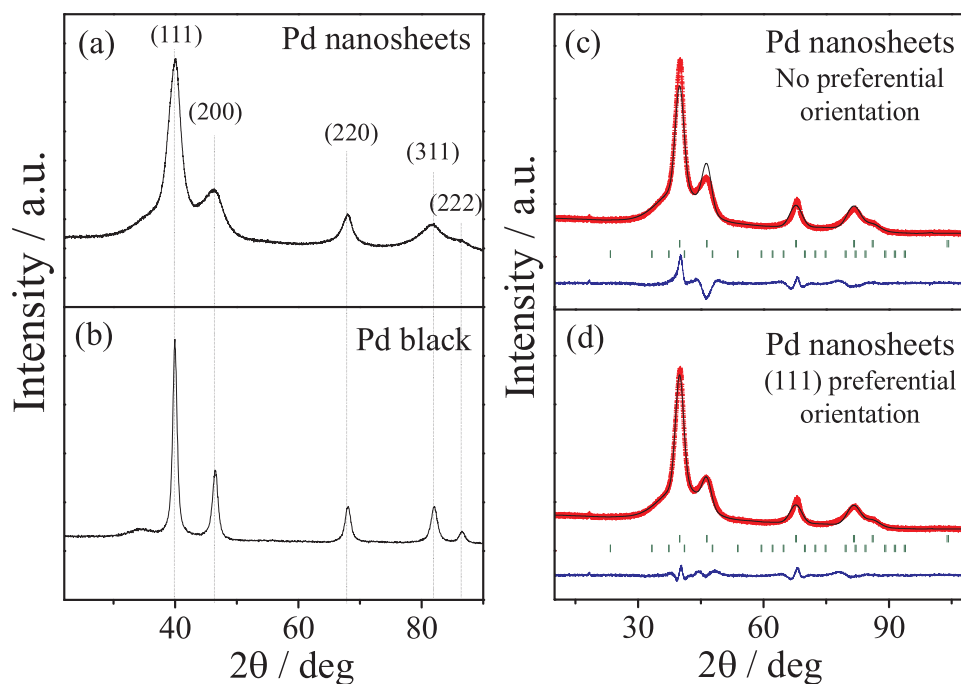


Fig. 1. X-ray diffractograms for (a) Pd-nanosheets and (b) Pd-black. Refinement of the crystal structure of Pd-nanosheets (c) without any preferential orientation and (d) oriented preferentially along the $\langle 111 \rangle$ direction.

planes. Fig. 1c shows the refinement obtained without including any preferential orientation. As observed, the refinement obtained shows that the calculated pattern does not explain all the scattering on the [111] reflection of the experimental pattern whereas the opposite effect is observed in the [200] reflection. On the other hand, the refinement shown in Fig. 1d was obtained by setting a preferential orientation of the Pd-nanosheets along the (111) plane. As observed, the refinement is noticeably improved when the (111) preferential orientation is included.

The morphology and structure of the Pd-nanosheets was thoroughly investigated using electron microscopy. Fig. S1 in the Supplementary information shows representative high resolution SEM images of the as prepared Pd-nanosheets. As observed, the specimens are composed by Pd-nanosheets exhibiting a 2D-structure with lateral size of ca. 5 nm (Fig. S1b). In general, the Pd-nanosheets display a roughly flat morphology although some curved sheets can be observed. A detailed study of the morphology and structure of the Pd-nanosheets was obtained by TEM/SAED. Fig. 2a shows the images of flat and curved Pd-nanosheets of ca. 1 μm length. Fig. 2b depicts the typical SAED pattern of Pd-nanosheets. The diffraction pattern reveals some intriguing features; for instance the reflections are strongly elongated along the azimuthal angle and, although less evident, along the radial direction. Moreover, taking into account that Pd-nanosheets is oriented along the [111] zone axis, as deduced by the presence of the (220) reflections (at 60°), it is puzzling to observe the set of reflections also at 60° and close to where the (111) reflections should appear. Thus, a complete indexation of the SAED is only possible if two set of reflections are taken into account. On the one hand, the reflections expected for a cubic Pd oriented down [111] are indicated by the red arrows in Fig. 2b. A further set of reflections resulting from an additional modulation wave vector of the type $\mathbf{q} = 1/3[422]$ are also visible and indicated by blue arrows in Fig. 2b. The presence of such a modulation wave vector has been previously described in the literature [43,44], and it is attributed to the presence of stacking faults parallel to the (111) planes. In this work, we assume that this is the correct model to explain the presence of the observed extra reflections to those in a perfect, undistorted, (111)* reciprocal plane as from a cubic Pd structure. Fig. 2c shows a HRTEM image of Pd-nanosheets in which the observation of lattice fringes of \approx

0.23 nm corroborate the presence of the $1/3$ [422] modulation wave vector. Note that the fringes are observed along all three equivalent directions according to the symmetry of the structure of Pd metal down this direction. The image shows also amorphous regions between the fringes containing domains, indicating that the origin of the threefold superstructure along [422] is probably an isolated domain superstructure rather than a perfectly well crystallized superstructure. In fact, the presence of planar defects, typically stacking faults, or nano-twins is clearly visible in Fig. 2d.

Fig. 2e shows that in some cases, Pd-nanosheets are covered by isolated Pd nanoparticles. The presence of such particles modifies the SAED patterns, which now show the expected diffractions for crystalline fcc Pd particles. Note that 200 and 222 reflections are clearly observed in the SAED pattern shown in the inset to Fig. 3d, but are absent in the SAED pattern of pure Pd-nanosheets (see Fig. 2b). Also note that the $1/3$ [422] reflections of the Pd-nanosheets are present but not observed since they are superimposed to the 111 reflections of polycrystalline Pd-nanoparticles.

The morphology of Pd-nanosheets is further clarified from STEM/HAADF images. As observed in Fig. 2f, Pd-nanosheets are actually formed by the stacking of several thinner sheets of Pd. Note that the individual Pd-nanosheets are not perfectly aligned and the edge of each layer is shifted, resulting in a stepped structure. The edge of each sheet is therefore exposed, thus resulting in a large fraction of Pd atoms in step/edges showing a quasi-hexagonal structure. As also observed, the steps and edges are indexable in terms of well-defined crystallographic planes. In the inset, we show a TEM image (inset to Fig. 2f) recorded at the edge one Pd-sheet revealing that the edges are defined by the (110) planes. This observation has been already reported for Au, Ag, and Pd platelets [45].

For comparison, Fig. 3 shows a representative micrograph of Pd-black. As observed, Pd particles in Pd-black have roughly globular shapes and are interconnected forming large aggregates. The mean size of the nanoparticles as deduced from the TEM images is of ca. 9–10 nm. The corresponding SAED pattern is shown in Fig. 3b, in which a higher magnification image is also shown. The particles are well crystalline and give rise to the electron diffraction pattern inset in the image characteristic of a polycrystalline sample.

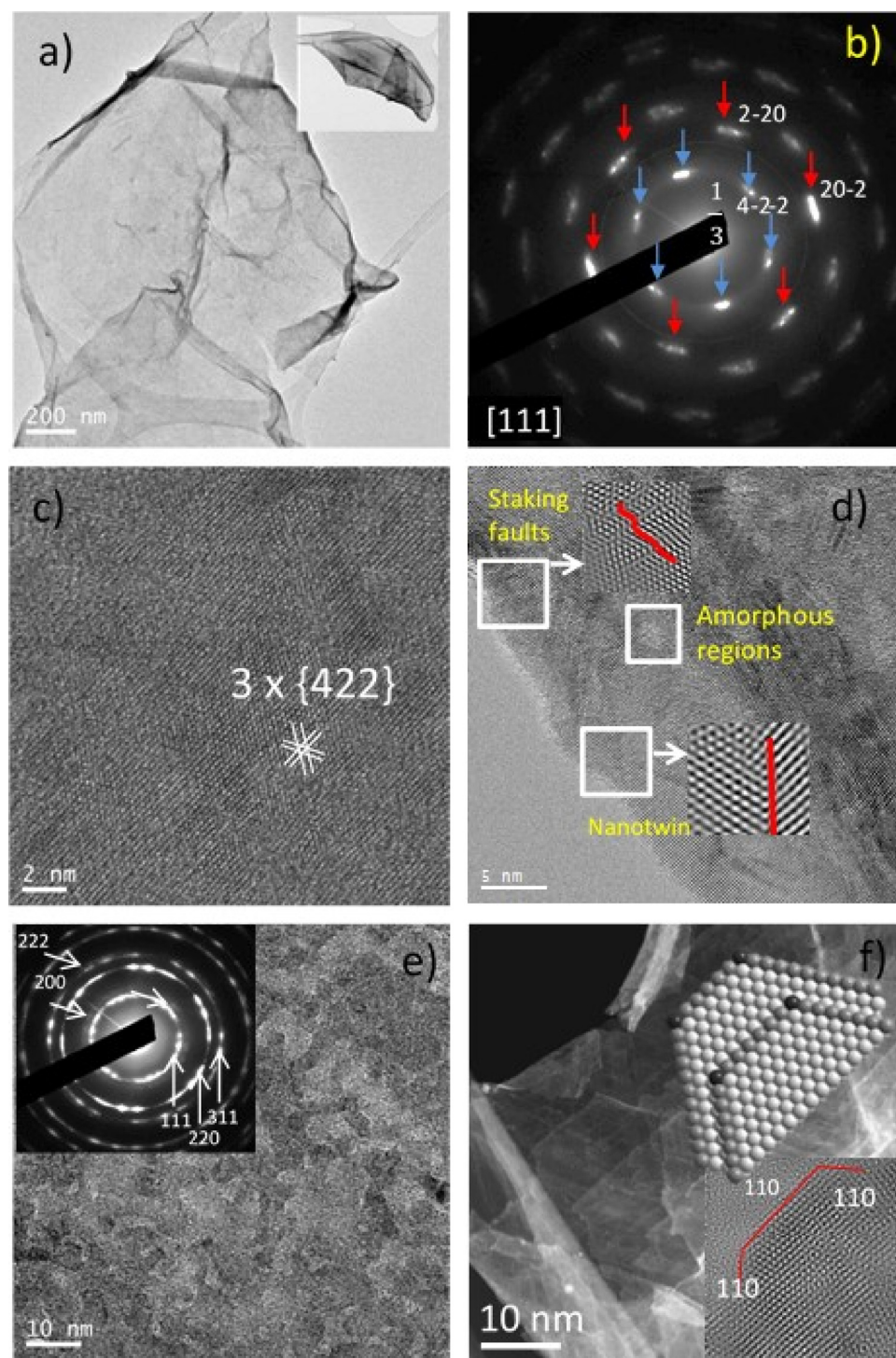


Fig. 2. a) Representative image Pd-nanosheets showing a flat morphology and, less frequently, curved shape (see inset); b) SAED pattern of Pd-nanosheets; red arrows identify reflections in the [111] direction of the cubic structure of Pd metal, blue arrows reflections with a modulation wave vector of the type $1/3[422]$; c) and d), HRTEM images showing the presence of defects, twins, stacking faults and amorphous regions; e) the presence of Pd nanoparticles deposited on the Pd-nanosheets and their SAED pattern (inset); f) STEM image of the Pd-nanosheets showing the stacking arrangement of the Pd-nanosheets and the exposure of steps and edges (with 110 terminations). Scheme of the layered structure of the Pd-nanosheets in which pale balls indicate atoms in 111 and dark ones indicate atoms in 110 planes. (For interpretation of the references to colour in this figure legend, the reader is referred to the web version of this article.)

Both XRD and TEM/SAED data reveal the preferential growth of the 2D planar Pd-nanosheets with (111) exposed surfaces. This behavior has been attributed to the use of CO as reducing agent in the synthesis [39]. This reducing agent prevents the 3D assembling of Pd along that direction, since CO is adsorbed on (111) surface, inhibiting the growth on that direction.

3.2. Electrochemical performance

Representative blank cyclic voltammograms for Pd-nanosheets and Pd-black between 0.25 and 1.45 V (vs RHE) are shown in Fig. 4a. The voltammograms are in line with the expected ones for Pd in alkaline

electrolyte, showing a H_{upd} adsorption/desorption region at low potentials and a Pd oxide formation/reduction region. As expected for Pd-based catalysts, it is possible to separate the H_{upd} and H absorption- H_{abs} desorption regions by recording cyclic voltammograms at lower potentials [46], see Fig. S2. The oxide formation/reduction region is characteristic of each sample. In line with previous observations, the onset potential of the Pd oxide formation region appears at relatively low potentials ca. 660 mV in Pd-nanosheets and Pd-black. A single oxide reduction peak is clearly observed at 558 and 663 mV in the voltammograms for Pd-nanosheets and Pd-black, respectively. As also observed in Fig. 4a, the charge associated with the oxide reduction of the Pd-nanosheets is significantly higher than that of Pd-black. Note

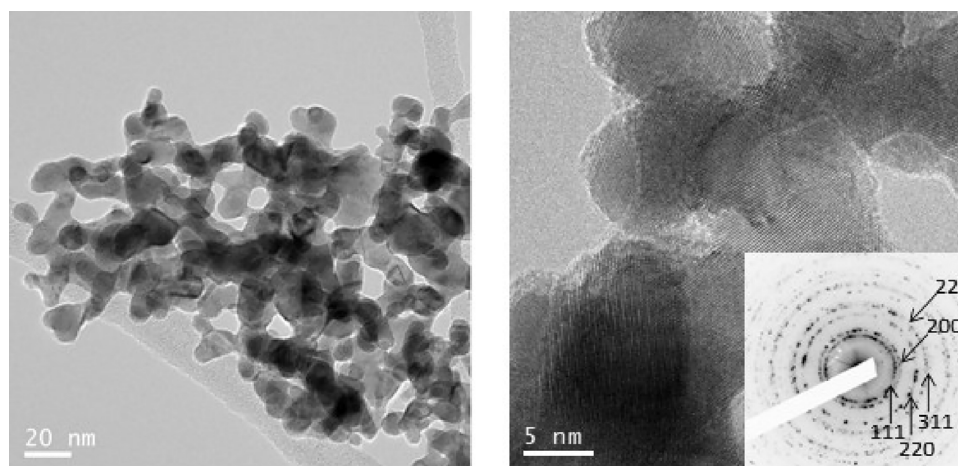


Fig. 3. a) TEM image of Pd-black showing the presence of globular shaped nano particles that agglomerate, b) HR-TEM image of Pd-black and SAED (inset) of the Pd particles.

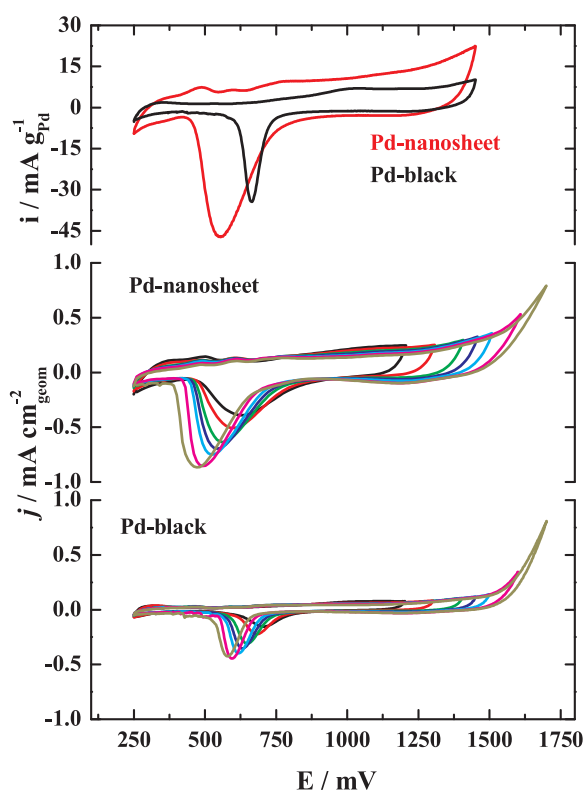


Fig. 4. Upper panel, cyclic voltammograms for Pd-nanosheets (black line) and Pd-black (red line) in 0.1 M KOH at 10 mV s⁻¹ with E_{inv} at 1450 mV. Central and lower panels, cyclic voltammograms for Pd-nanosheets and Pd-black at different E_{inv} from 1200 to 1700 mV. (For interpretation of the references to colour in this figure legend, the reader is referred to the web version of this article.)

that Pd loading on both electrodes is the same (in addition CVs are normalized to the actual Pd loading on the electrode). This feature suggests a higher dispersion *i.e.*, the ratio between surface and bulk Pd atoms, in Pd-nanosheets than in Pd-black.

Several approaches for the evaluation of electrocatalytic surface area (ECSA) of metallic particles exist. The evaluation of H_{upd} is typically used for Pt-based catalysts; however, the ability of Pd for hydrogen absorption within the H_{upd} region precludes the accurate estimation of ECSA from the H_{upd} region. The evaluation ECSA from the CO_{ad} stripping charge on Pd can be also problematic because the

multiple modes of CO adsorption on Pd hampers the determination of the actual Pd/ CO_{ad} stoichiometry. For further discussion on this topic see [47] and references therein. The most extended approach to determine ECSA is the integration of the Pd oxide reduction charge [48,49]. However, the values obtained from this approach should be also taken carefully, since the actual charge of the Pd oxide reduction peak depends on the upper limit of the positive going scan, *i.e.*, the inversion potential (E_{inv}).

This is because features such as the formation of Pd-oxides with different stoichiometries, oxygen absorption within Pd, and Pd dissolution and/or agglomeration prevent an accurate identification of the actual Pd–O stoichiometry [47]. As a consequence, ECSA values for the Pd samples obtained from the integration of the oxide region should be reported by indicating the actual E_{inv} at which they were obtained. This feature is clearly illustrated in Fig. 4b and c showing the cyclic voltammograms for Pd-nanosheets and Pd-black recorded from 250 mV to E_{inv} ranging between 1200 and 1700 mV. As observed, the area of the oxide reduction peak increases with the increasing E_{inv} .

The charges associated to the oxide reduction processes recorded at every E_{inv} , have been used for the estimation of the ECSA of both catalysts. Actual ECSA values have been obtained by using Eq. (1) and assuming that the charge associated for the reduction of a monolayer of PdO is of 405 $\mu C cm^{-2}$ [50].

$$ECSA \left(\frac{cm^2}{g} \right) = \frac{Q_{measured} (\mu C)}{Q_{monolayer} \left(\frac{\mu C}{cm^2} \right) * mass_{Pd, electrode} (g)} \quad (1)$$

Pd surface the ECSA values obtained at every E_{inv} are reported in Table 1.

As observed, Pd area and therefore ECSA values of both Pd-nanosheets and Pd-black increase with the increasing E_{inv} . In addition, the ECSA values of the Pd-nanosheets are larger than those of Pd-black. It is

Table 1

Evolution of surface area (cm^2) and ECSA ($m^2 g_{Pd}^{-1}$) with E_{inv} between 1200 and 1700 mV for Pd-nanosheets and Pd-black.

E_{inv} / mV	Pd-nanosheets		Pd-black	
	Pd area / cm^2	ECSA / $m^2 g_{Pd}^{-1}$	Pd area / cm^2	ECSA / $m^2 g_{Pd}^{-1}$
1200	17.7	132	4.8	36
1300	22.0	164	5.5	41
1400	26.0	194	7.2	53
1500	26.8	200	8.0	59
1600	30.0	223	8.5	63
1700	31.5	234	9.2	68

also important to remark that the $\text{ECSA}_{\text{Pd-nanosheets}}/\text{ECSA}_{\text{Pd-black}}$ is ~ 3.6 , regardless of E_{inv} .

The mass specific surface area (A_s) of metallic particles can be also calculated from the size of particles as determined by TEM, as shown in Eq. (2) [51].

$$A_s = \sum \pi d^2 / \sum \frac{1}{6} \rho \pi d^3 = 6 \sum d^2 / \rho \sum d^3 = 6 / \rho d_{v/a} \quad (2)$$

Where d is the average diameter of the particles as calculated by TEM and ρ is the bulk density of Pd (fcc) as:

$$\rho = \frac{Mw \times Z}{N_A \times V_{f.u.}} \quad (3)$$

where Mw is the molecular weight, Z is the number of formula units per cell ($Z = 4$ for $Fm\bar{3}m$), N_A is the Avogadro's number and $V_{f.u.}$ is the volume of the formula unit.

The surface area (A_s) of Pd-black is $50 \text{ m}^2/\text{g}$. This value is in line with the ECSA values obtained for Pd-black that range between 36 and $68 \text{ m}^2/\text{g}$ depending of the E_{inv} . In particular, the best agreement is found with the ECSA value of $53 \text{ m}^2/\text{g}$ obtained at E_{inv} of 1400 mV. As observed in Table 1, the ECSA of the Pd-nanosheets at E_{inv} of 1400 mV is of $194 \text{ m}^2/\text{g}_{\text{Pd}}$. ECSA values at E_{inv} 1400 mV were used for determining the intrinsic activity for the EOR. Note that is not possible to calculate the A_s value for Pd-nanosheets since it is not possible to calculate d for Pd-nanosheets from TEM images since Pd particles are not spherical.

3.3. Electrooxidation of ethanol

Fig. 5 shows the cyclic voltammograms recorded during ethanol electrooxidation. The voltammograms for all samples demonstrate the ability of Pd-based catalysts towards ethanol oxidation by showing strong oxidation waves in the forward scan, with E_p at ca. 990 mV for Pd-nanosheets and ca. 850 mV for Pd-black. As observed, the oxidation wave of Pd-nanosheets is significantly higher than that observed for Pd-black (note that Pd loading on both electrodes is the same). The onset potential for the electrooxidation of ethanol is observed at ca. 350 mV for Pd-nanosheets shifting to higher potentials for Pd-black. In the reverse scan an oxidation process (as expected from the irreversible electrooxidation of ethanol) is also observed. The onset potential of the reverse wave coincides well the onset potential for the reduction of PdO

process.

Not only Pd-nanosheets delivers higher current density than Pd-black ($i_p \sim 150$ vs 30 mA g^{-1}) (CVs normalized to the Pd loading are shown in Fig. S3), but also a lower overpotential for the EOR is clearly observed. Both observations indicate the superior ability of Pd-nanosheets for the EOR. This might be attributed to the following reasons: i) the 2D sheet-like structure of Pd-nanosheets results in a higher fraction of exposed Pd atoms, i.e., higher electrochemical surface area (ECSA) and/or ii) the presence of sites with higher intrinsic activity for the EOR in Pd-nanosheets. In addition, the EOR activity of Pd-nanosheets is better than that of representative pure Palladium nanostructures, for instance chestnut-bur-like palladium [52] or Raney-like nanoporous Pd [21]. It is worth noting that the 2D morphology of the Pd-nanosheets remains constant after the OER, see Fig. S4.

In order to assess the intrinsic activity of both catalysts for the EOR, the activity was normalized to the ECSA values obtained for the integration of the oxide reduction peaks of the voltammograms recorded at E_{inv} of 1.4 V, see Table 1. As shown in Fig. 5b, the intrinsic activity (in mA cm^{-2}) of the Pd-nanosheets for the EOR is still higher than that of Pd-black. This observation indicates that, in addition of displaying a higher fraction of exposed Pd atoms, more active sites for the EOR are present in Pd-nanosheets than in Pd-black. As discussed above (see XRD and TEM results), the particular layered arrangement of the Pd-nanosheets results in a preferential exposure of 111 planes along with a high fraction of atoms located in low coordination sites (kinks, steps, edges). The beneficial role of defects for the EOR with Pt catalysts in acid electrolyte has been reported [53]. Although similar studies with Pd-based catalysts in alkaline electrolyte are scarcer, it has been reported that Pt 111 is more active than Pt 100 or 110 for the EOR in NaOH [54]. As discussed above, XRD and TEM results reveal a preferential exposure of 111 planes in Pd-nanosheets, thus explaining the observed high EOR activity.

3.4. In situ FTIR spectroscopy measurements

Fig. 6a and b show selected regions of the IR spectra (the IR spectra between 4000 and 1150 cm^{-1} are shown in Fig. S5) recorded during ethanol oxidation (EOR) in $\text{H}_2\text{O}/\text{KOH}$ and $\text{D}_2\text{O}/\text{KOD}$ electrolytes, respectively. As discussed in reference [9], spectra recorded in H_2O electrolytes are dominated by the strong IR features of H_2O at

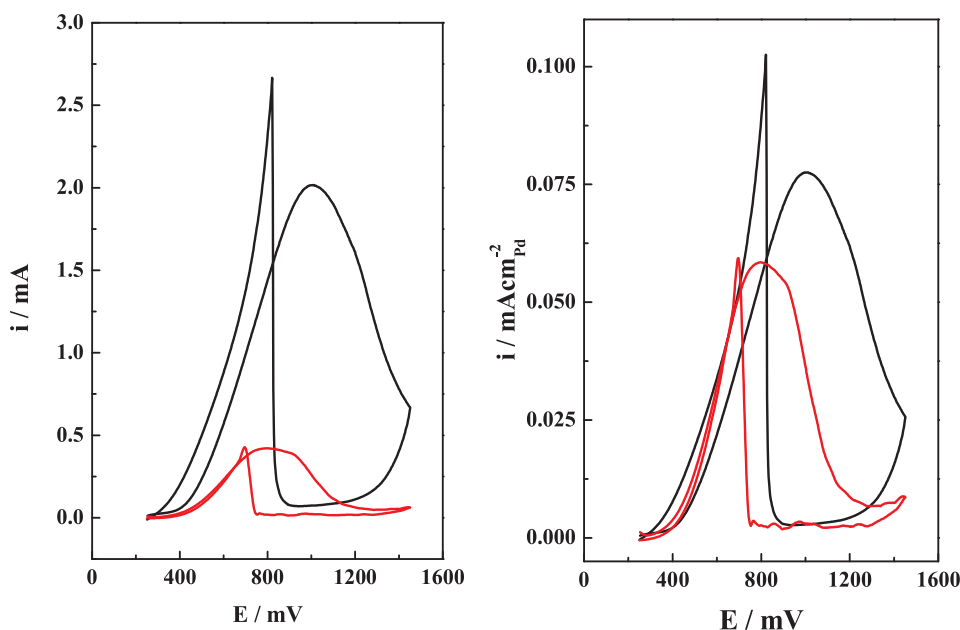


Fig. 5. Cyclic voltammograms (1st cycle) recorded during ethanol oxidation ($0.5 \text{ M C}_2\text{H}_5\text{OH}$ in 0.1 M KOH) at 10 mV s^{-1} for Pd-nanosheets (black) and Pd-black. a) current density (j) as normalized to geometric area of the electrode; b) current normalized to ECSA values obtained at $E_{\text{inv}} = 1.4 \text{ V}$.

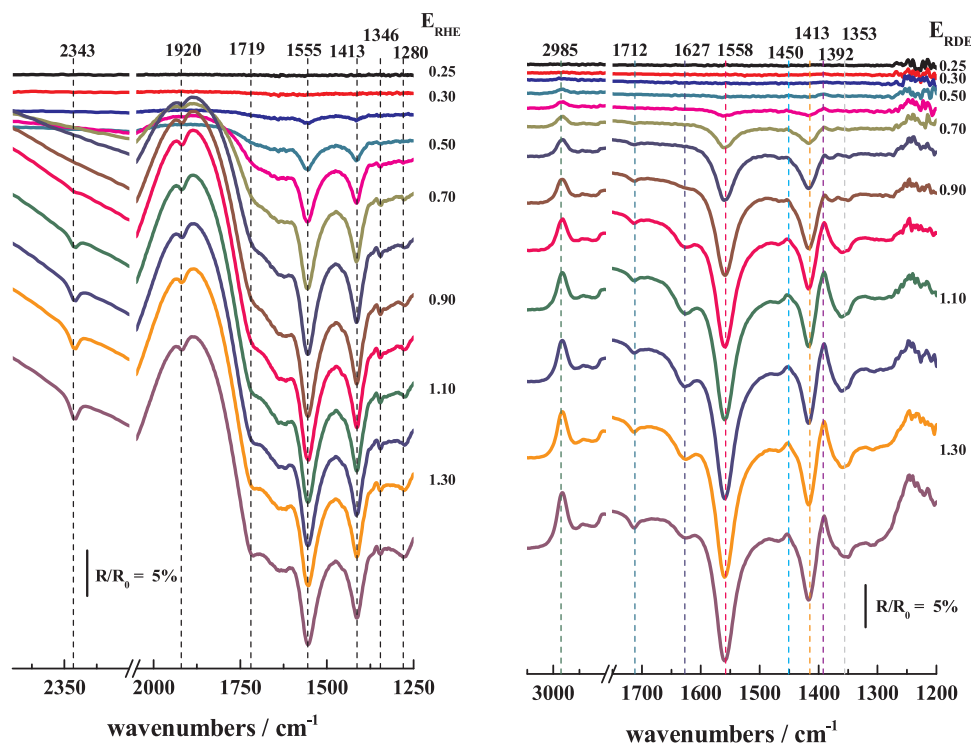


Fig. 6. IR spectra for Pd-nanosheets recorded during a LSV between 250 and 1450 mV at 1 mV s^{-1} in a) $0.5 \text{ M C}_2\text{H}_5\text{OH}$ in 0.1 M KOH in H_2O and b) $\text{C}_2\text{H}_5\text{OH}$ in 0.1 M KOH in D_2O .

3270 cm^{-1} (O–H stretch) and 1635 cm^{-1} (HOH deformation), and of OH^- at 2750 and 1870 cm^{-1} . On the other hand, a strong D_2O band appears at 1200 cm^{-1} and the vibrational band ν_{OD} appears at between 2400 and 2600 cm^{-1} . The frequency and assignment of the bands is collated in Table S1.

As observed in Fig. 6a, the spectra recorded in the H_2O -electrolyte are dominated by the strong positive going OH^- feature at ca. 1870 cm^{-1} (a very strong negative band at ca. 2700 cm^{-1} is also observed in the spectra, see Fig. S5). The IR spectra recorded at $E \geq 400 \text{ mV}$ during EOR in $\text{KOH}/\text{H}_2\text{O}$ show two main negative going bands at 1413 and 1555 cm^{-1} ; as observed, the intensity of the high frequency band is slightly higher than that of low frequency one, but their relative intensity remains similar with the potential. These peaks are characteristic of the symmetric and asymmetric stretching modes of the O–C–O group of acetate ions. The observation of both the asymmetric and symmetric vibrational modes indicates that acetates are in solution rather than adsorbed, since, due to selection rules, the asymmetric stretch of bidentate acetate would not be observed [55].

The spectra recorded at $E \geq 500 \text{ mV}$ show a weak negative going feature at 1346 cm^{-1} . This band is usually ascribed to the bending vibrations of the $-\text{CH}_3$ group of acetates in solution [56], although some authors ascribed it to adsorbed acetates [55] or acetaldehyde [57]. A careful inspection of this peak, reveals the presence of a weak positive going feature at 1357 cm^{-1} . In fact, it is difficult to discriminate whether the peaks at 1346 and 1357 cm^{-1} are actually two individual features or a bipolar band. In addition, a very weak positive going band at ca. 1382 cm^{-1} is also observed in the spectra. Shao et al. ascribed a band at ca. 1350 cm^{-1} to CH_3 of acetates adsorbed on Pt [55], whereas bands at ca. 1380 cm^{-1} are usually ascribed to carbonates.

The spectra recorded at $E \geq 800 \text{ mV}$ show two weak bands at ca. 1280 and 1719 cm^{-1} ascribed to acetic acid and acetaldehyde in solution, respectively [55]. A further negative going band at 2343 cm^{-1} is observed in the spectra at $E \geq 1000 \text{ mV}$ and assigned to CO_2 in solution. Those species are not stable in alkaline electrolyte and their observation is indicative of the acidification of the environment (pH lower than 6.37), a feature previously observed by other authors [58–60].

Note that in the spectroelectrochemical cells typically used for these experiments the electrolyte is constrained within a thin layer between the working electrode and the prism so that the rate of OH^- consumption during the EOR is faster than the diffusion of KOH from the bulk, thus resulting in a progressive increase of pH with the increasing potential. The observation of CO_2 clearly indicates the scission of the C–C bond and the total oxidation of ethanol. In general, this process is preceded by the formation of CO_{ad} species; however, the identification of this species during EOR in alkaline electrolyte is not straightforward. Zhou et al. and Yang et al. identified bridged bonded CO on Pd disks or Pd films from a IR feature at 1835 cm^{-1} [27,58]. Lai et al. reported the presence of linearly and bridged CO_{ad} species on Pt during EOR in alkaline at 2050 and ca. 1820 cm^{-1} [57]. On the other hand, other authors have failed to identify CO_{ad} species during EOR with Pd/C, and ascribed it to the rapid oxidation of CO_{ad} to CO_2 [61]. The spectra recorded at $E \geq 800 \text{ mV}$ clearly show the presence of a weak negative going band at 1920 cm^{-1} that can be ascribed to bridged bonded CO on Pd. Sadly, the accurate identification of the position and shape of this band is hampered by the very strong positive going feature of OH^- . On the other hand, carbonates (CO_3^{2-}) are the stable species of the total oxidation of ethanol in alkaline media. The presence of CO_3^{2-} is characterized by an IR band between ca. 1390 – 1370 cm^{-1} [56,58,62] whereas the presence of HCO_3^- results in a band at ca. 1319 cm^{-1} [57]. As stated above, a small positive going feature at 1380 cm^{-1} is observed in the spectra (at $E \geq 500 \text{ mV}$) which suggests that carbonates are formed at the potential at which the reference spectrum was acquired.

The spectra recorded in $\text{KOD}/\text{D}_2\text{O}$ are shown in Fig. 6b. Due to the lack of IR features from H_2O , the IR region between 1600 and 1400 cm^{-1} is better defined. In line with the spectra recorded in H_2O , the spectra recorded during the EOR are dominated by two negative going bands at 1413 and 1558 cm^{-1} , assigned to the symmetric and asymmetric stretching modes of the O–C–O group of acetate ions in solution. However, some differences between the spectra recorded in $\text{KOH}/\text{H}_2\text{O}$ and $\text{KOD}/\text{D}_2\text{O}$ can be observed. In line with the spectra recorded in $\text{KOH}/\text{H}_2\text{O}$, the intensity of both bands is similar in the spectra

recorded in KOD/D₂O at low potentials. However, the intensity of the band at 1558 cm⁻¹ appears to increase faster than that of the band at 1413 cm⁻¹ with the increasing potential in the spectra recorded in the deuterated electrolyte. The apparent smaller intensity of the low frequency band could be related with the appearance of a positive going band at 1392 cm⁻¹ that overlaps with the band at 1413 cm⁻¹ thus resulting in an apparent decreasing of the intensity of the band at 1413 cm⁻¹ (and probably also of the band at 1392 cm⁻¹). A careful inspection of the spectra reveals that the positive going band at 1392 cm⁻¹ can be actually observed, as a weak band, in the spectra recorded at $E \geq 400$ mV, and its intensity increases with the applied potential. As stated above, the band at 1392 cm⁻¹ is ascribed to carbonates [58], which are the stable species of the total oxidation of ethanol in alkaline electrolyte. Remarkably, the fact that this is a positive going band indicates that carbonates are actually formed during the acquisition of the reference spectrum at 250 mV, i.e., the total oxidation of ethanol takes place at a relatively low potential at the surface of Pd-nanosheets. This feature will be discussed below.

The spectra recorded in KOD/D₂O also show a series of high frequency positive going bands at 2985 and 2840 cm⁻¹ due to C–H vibrations and that account to the disappearance of ethanol during the EOR. In addition, two negative going bands at 1712 and 1627 cm⁻¹ are clearly observed in the spectra at $E \geq 800$ mV. The first band is ascribed to dissolved acetaldehyde (in acid electrolyte) whereas the latter one has been ascribed to the C=O stretching of adsorbed acetaldehyde or acetyl species [55]. The observation of these bands is indicative of the acidification of the electrolyte as discussed above.

As stated above, one of the most significant features observed in the spectra recorded in the deuterated electrolyte is the presence and evolution of the band at 1392 cm⁻¹. This band is ascribed to carbonates, and therefore is an indication of the total oxidation of ethanol. More importantly, the fact that it is a positive going band indicates that carbonates are already formed at the potential at which the reference spectrum was collected, i.e., 250 mV. Note that the collection of a stable reference spectrum takes at least 60 min under 250 mV. The ability of Pt for C–C scission and CO₂ formation at low potentials in acid electrolyte has been reported previously [9,10,63]. These studies suggests that upon ethanol adsorption two reaction pathways are possible depending on the nature of the catalyst surface. When adsorbed on metallic surfaces the C–C scission of the ethanol, i.e., the C1 pathway, is possible. On the other hand, at potentials where the catalyst surface is covered by OH_{ad} species, the partial oxidation of ethanol to acetic acid is the preferred pathway. Therefore, C–C scission is favored at low potentials whereas the partial oxidation of ethanol is favored at potentials sufficiently high to nucleate OH_{ad} species.

In order to corroborate whether this approach also applies to alkaline electrolyte we have collected IR spectra during EOR in KOD/D₂O electrolyte by recording the reference spectrum at 30 mV and applying a step program potential between 30 and 250 mV with ΔE 10 mV keeping each potential during ca. 6 min, so that at least 2 IR spectra can be collected at each potential, see Fig. 7a. Finally, a linear sweep potential program between 250 and 1450 mV at 5 mVs⁻¹ is applied while recording IR spectra. Fig. 7b shows selected IR spectra recorded during this potential program.

The spectra shown in Fig. 7a show a series of negative going bands at 1453, 1391, and 1368 cm⁻¹; as observed, their intensity increases with both time and potential. The band at 1391 cm⁻¹ is ascribed to carbonates and as observed, its intensity increases with the increasing potential. Clearly, the observation of carbonates at potentials as low as 30 mV clearly indicates that ethanol adsorption and C–C scission take place at the surface of the Pd-nanosheets at low potentials, previous to nucleation of OH_{ad}. CO_{ad} oxidation to CO₂ (or carbonates in alkaline electrolyte), proceeds through a Langmuir-Hinshelwood (H–L) like mechanism, i.e., the presence of vicinal CO_{ad} and OH_{ad} species. Whereas at low potentials OH nucleation does not take place, it has been reported that a (small) fraction of reactive OH species are

adsorbed at defects in the 111 surface of Pt in NaOH [64]. Taking into account that Pd-nanosheet have a large fraction of Pd atoms in steps and edges, a non-zero coverage of OH at low positive potentials is expected. Moreover, CO_{ad} oxidation in alkaline can also proceed through an Eley-Rideal mechanism (E–L) [64–66] whereby CO_{ad} reacts with non-adsorbed OH_x species in the electrolyte (in the outer Helmholtz plane, OHP). It should be taken into account that by conducting the reaction at high pH, the presence of an excess of OH⁻ ions in the outer sphere is expected at any potential, thus favoring the E–R pathway.

The assignment of the bands at 1453 and 1368 cm⁻¹ is less evident. First, the presence of a (very) weak band at ca. 1450 cm⁻¹ has been reported by several authors and ascribed to bending modes of –CH₃ groups [27,61]. However, the band at 1453 cm⁻¹ in the spectra in Fig. 7a is (very) strong, which indicates that this band arises from a different species. We have tentatively assigned the band at 1453 cm⁻¹ to acetate adsorbed through one single oxygen atom to Pd (Pd–O–C(O)–CH₃) and the band at 1368 cm⁻¹ to the bending the CH₃ group of adsorbed acetates (note the similar evolution of both bands with time and potential in spectra 7a and 7b). As discussed above, due to selection rules the asymmetric stretch of bidentate acetate would not be observed [55]. Our proposal is in line with Christensen et al., who based upon the observation of IR bands at 1573 and 1475 cm⁻¹ suggest the formation of monodentate adsorbed acetates on Pt electrodes (Pt–CH₂(CO)O–Pt) during the EOR in alkaline electrolyte [56].

Fig. 7b shows the spectra collected during LSV at 5 mVs⁻¹ from 250 to 1450 mV, that is, immediately after the last spectrum shown in Fig. 7a was collected. As observed in Fig. 7b, the spectra collected at ca. $E \leq 500$ mV are similar to that recorded at 250 mV; however, major changes are observed at $E \geq 700$ mV. Thus, in addition to the bands observed at lower potentials, the spectra at 700 mV show three main bands at ca. 1560, 1416, and 1347 cm⁻¹. In line with previous assignments, the latter bands are ascribed to the asymmetric, symmetric and to the bending of CH₃ of acetates in solution.

As observed in Fig. 7b, the intensity of the bands at 1391, 1453, and 1368 cm⁻¹ decreases with the increasing potential, especially at $E \geq 700$ mV. This feature indicates that carbonates, and adsorbed acetates disappear with the increasing potential. The disappearance of the adsorbed acetates accounts to desorption and dissolution, resulting in the increasing of the concentration of dissolved acetates, in line with the increasing intensity of the bands at ca. 1560 and 1416 cm⁻¹, as observed in Fig. 7b. On the other hand, the disappearance of carbonates can be explained by the acidification of the electrolyte during the EOR, and the subsequent transformation of carbonates into CO₂ (note that CO₂ bands are not observed in D₂O containing electrolytes, but are clearly observed in the spectra recorded in H₂O as shown in Fig. 6a). In fact, the acidification of the electrolyte is further confirmed from the observation of the bands at 1715 and 1631 cm⁻¹ characteristic of the carbonyl groups of acetaldehyde and/or acetyl species (see above).

Adsorbed acetyls have been postulated by several authors as the precursor species for the scission of the C–C bond of ethanol in acid electrolyte [55,67]; although IR studies conducted in deuterated electrolytes fail to observe the presence of acetyls [9,68]. The contribution of acetyls to the EOR in alkaline is controversial; whereas experimental studies suggest that they participate in the C2 pathway [27], theoretical studies postulate acetyls as a pivotal intermediate species for C–C scission during EOR [61]. The spectra in Figs. 6 and 7 recorded in D₂O clearly show a band at ca. 1631 cm⁻¹ which is assigned to the formation of acetyl species. However, it should be noted that this band is only observed as a negative going band (appearing species) in the spectra recorded at high potentials ($E \geq 900$ mV), i.e., after neutralization/acidification of the electrolyte. Despite the presence of carbonates indicate the scission of the C–C bond, we have found no evidences of the formation of acetyls at low potentials, questioning the participation of acetyls in the C1 pathway.

The results shown above clearly demonstrate that Pd-nanosheets are very active catalysts for the EOR in alkaline electrolyte. Their high EOR

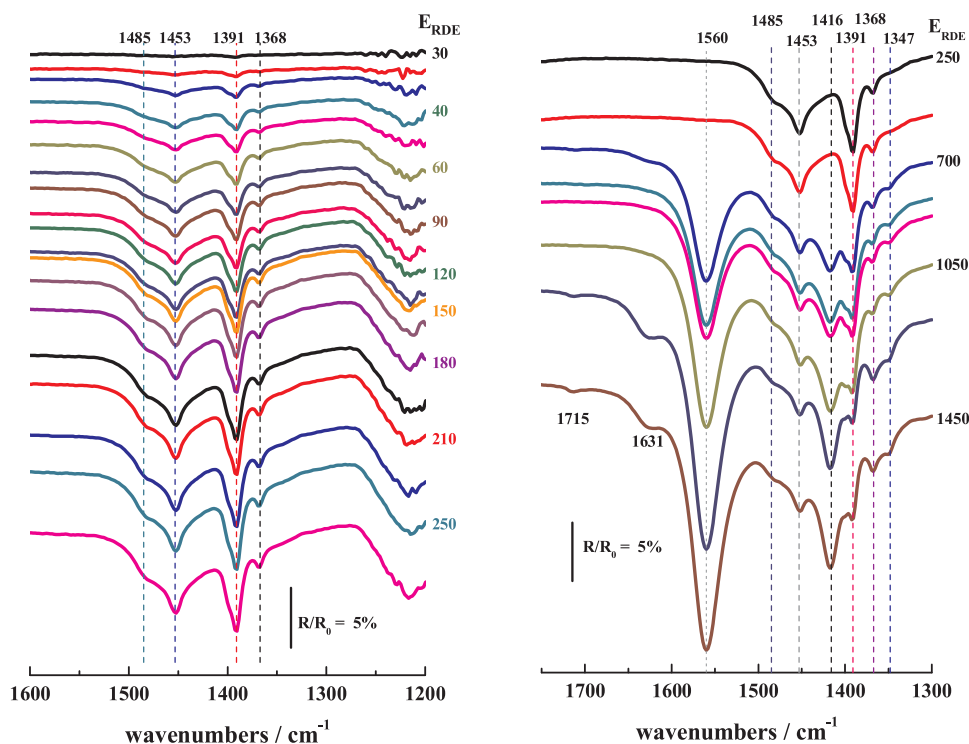


Fig. 7. IR spectra during EOR in 0.1 M KOD in D₂O using a reference spectrum collected at 30 mV. a) spectra acquired during a step potential program at E = 30, 40, 60, 90, 120, 150, 180, 210, and 250 mV. b) spectra acquired during a LSV between 250 and 1450 mV s⁻¹ at 5 mV s⁻¹.

activity accounts to the very active surface area resulting from the very high surface exposure imposed by the 2D structure of the Pd-nanosheets and to the preferential exposure of Pd atoms in 111 planes. The infrared spectra collected during the EOR suggest that the partial oxidation of ethanol to acetates is the main reaction pathway, especially at high potentials where the surface of Pd atoms is covered by OH_{ad} species. However, the total oxidation of ethanol to C1 species is observed at low potentials, where the metallic surface of Pd is able to break the C–C bond.

4. Conclusions

2D Pd-nanosheets have been synthesized by a simple chemical method using CO as reducing agent. The Pd-nanosheets obtained exhibit a 2D-like morphology with a high fraction of Pd surface atoms. The ECSA values obtained by integration of the reduction charge of the Pd-oxide peak range between ca. 130 and 240 m²/g_{Pd}, depending on the E_{inv}. The ESCA value of 194 m²/g_{Pd} (E_{inv} of 1400 mV) was selected as the most representative value for Pd-nanosheets and used to determine intrinsic activities for the EOR. In addition, a preferential exposure of the Pd 111 facets along with a high fraction of Pd atoms in steps and edges is also observed. As a result Pd-nanosheets exhibit very high activity for the electrooxidation of ethanol in alkaline electrolyte, showing ca. 5 times higher activity than commercial Pd nanoparticles. In situ infrared spectra recorded during the EOR show that carbonates are formed at low potentials (ca. 30 mV). This observation indicates that Pd-nanosheets are capable of breaking the C–C bond of ethanol in the metallic state, before the nucleation of OH_{ad} species at the surface of Pd takes place. On the other hand, acetates are the main reaction product at potentials higher than 250 mV, and the scission of the C–C bond of ethanol is very limited at potentials above 250 mV.

Acknowledgements

Dr. Francisco Javier García-García is acknowledged for his help with the discussion of results. This work was supported by Projects

ENE2016-77055-C3-3-R from Ministerio de Economía, y Competitividad from Spain, and PIE 201480E122 from CSIC.

Appendix A. Supplementary data

Supplementary material related to this article can be found, in the online version, at doi:<https://doi.org/10.1016/j.apcatb.2018.06.051>.

References

- [1] E. Antolini, Catalysts for direct ethanol fuel cells, *J. Power Sources* 170 (2007) 1–12.
- [2] G.A. Camara, T. Iwasita, Parallel pathways of ethanol oxidation: the effect of ethanol concentration, *J. Electroanal. Chem.* 578 (2005) 315–321.
- [3] S. García-Rodríguez, T. Herranz, S. Rojas, Electrocatalysts for the Electrooxidation of Ethanol, *New and Future Developments in Catalysis: Batteries, Hydrogen Storage and Fuel Cells*, Elsevier B.V., 2013, pp. 33–67.
- [4] N.V. Long, Y. Yang, C. Minh Thi, N.V. Minh, Y. Cao, M. Nogami, The development of mixture, alloy, and core-shell nanocatalysts with nanomaterial supports for energy conversion in low-temperature fuel cells, *Nano Energy* 2 (2013) 636–676.
- [5] A. Cuña, C. Reyes Plascencia, E.L. da Silva, J. Marcuzzo, S. Khan, N. Tancredi, M.R. Baldan, C. de Fraga Malfatti, Electrochemical and spectroelectrochemical analyses of hydrothermal carbon supported nickel electrocatalyst for ethanol electro-oxidation in alkaline medium, *Appl. Catal. B: Environ.* 202 (2017) 95–103.
- [6] M.D. Obradović, Z.M. Stančić, U.Č. Lačnjevac, V.V. Radmilović, A. Gavrilović-Wohlmuter, V.R. Radmilović, S.L. Gojković, Electrochemical oxidation of ethanol on palladium-nickel nanocatalyst in alkaline media, *Appl. Catal. B: Environ.* 189 (2016) 110–118.
- [7] J. Guo, R. Chen, F.-C. Zhu, S.-G. Sun, H.M. Villullas, New understandings of ethanol oxidation reaction mechanism on Pd/C and Pd₂Ru/C catalysts in alkaline direct ethanol fuel cells, *Appl. Catal. B: Environ.* 224 (2018) 602–611.
- [8] W. Hong, J. Wang, E. Wang, Facile synthesis of highly active PdAu nanowire networks as self-supported electrocatalyst for ethanol electrooxidation, *ACS Appl. Mater. Interfaces* 6 (2014) 9481–9487.
- [9] J. Torrero, F.J. Pérez-Alonso, M.A. Peña, C. Domínguez, A.O. Al-Youbi, S.A. Al-Thabaiti, S.N. Basahel, A.A. Alshehri, S. Rojas, In situ infrared study of the electrooxidation of ethanol and acetaldehyde in acid electrolyte, *ChemElectroChem* 3 (2016) 1072–1083.
- [10] R. Kavanagh, X.-M. Cao, W.-F. Lin, C. Hardacre, P. Hu, Origin of low CO₂ selectivity on platinum in the direct ethanol fuel cell, *Angew. Chem. Int. Ed.* 51 (2012) 1572–1575.
- [11] H. Xu, B. Yan, K. Zhang, C. Wang, J. Zhong, S. Li, Y. Du, P. Yang, PVP-stabilized PdAu nanowire networks prepared in different solvents endowed with high

- electrocatalytic activities for the oxidation of ethylene glycol and isopropanol, *Colloids Surf. A: Physicochem. Eng. Asp.* 522 (2017) 335–345.
- [12] Y. Zhang, G. Chang, S. Liu, J. Tian, L. Wang, W. Lu, X. Qin, X. Sun, Microwave-assisted, environmentally friendly, one-pot preparation of Pd nanoparticles/graphene nanocomposites and their application in electrocatalytic oxidation of methanol, *Catal. Sci. Technol.* 1 (2011) 1636–1640.
 - [13] S. García-Rodríguez, M.A. Peña, J.L.G. Fierro, S. Rojas, Controlled synthesis of carbon-supported Pt₃Sn by impregnation-reduction and performance on the electrooxidation of CO and ethanol, *J. Power Sources* 195 (2010) 5564–5572.
 - [14] S. García-Rodríguez, F. Somodi, I. Borbáth, J.L. Margitfalvi, M.A. Peña, J.L.G. Fierro, S. Rojas, Controlled synthesis of Pt-Sn/C fuel cell catalysts with exclusive Sn-Pt interaction: application in CO and ethanol electrooxidation reactions, *Appl. Catal. B: Environ.* 91 (2009) 83–91.
 - [15] T. Herranz, M. Ibáñez, J.L. Gómez de la Fuente, F.J. Pérez-Alonso, M.A. Peña, A. Cabot, S. Rojas, In situ study of ethanol electrooxidation on monodispersed Pt₃Sn nanoparticles, *ChemElectroChem* 1 (2014) 885–895.
 - [16] S. Gottesfeld, D.R. Dekel, M. Page, C. Bae, Y. Yan, P. Zelenay, Y.S. Kim, Anion exchange membrane fuel cells: current status and remaining challenges, *J. Power Sources* 375 (2018) 170–184.
 - [17] Y. Kwon, S.C.S. Lai, P. Rodríguez, M.T.M. Koper, Electrocatalytic oxidation of alcohols on gold in alkaline media: base or gold catalyst? *J. Am. Chem. Soc.* 133 (2011) 6914–6917.
 - [18] A.N. Geraldes, D. Furtunato da Silva, J.C. Martins da Silva, O. Antonio de Sá, E.V. Spinacé, A.O. Neto, M. Coelho dos Santos, Palladium and palladium–tin supported on multi wall carbon nanotubes or carbon for alkaline direct ethanol fuel cell, *J. Power Sources* 275 (2015) 189–199.
 - [19] J.B. Xu, T.S. Zhao, Y.S. Li, W.W. Yang, Synthesis and characterization of the Au-modified Pd cathode catalyst for alkaline direct ethanol fuel cells, *Int. J. Hydrogen Energy* 35 (2010) 9693–9700.
 - [20] S. Li, J. Ma, H. Huo, J. Jin, J. Ma, H. Yang, Ionic liquids-noncovalently functionalized multi-walled carbon nanotubes decorated with palladium nanoparticles: a promising electrocatalyst for ethanol electrooxidation, *Int. J. Hydrogen Energy* 41 (2016) 12358–12368.
 - [21] X. Wang, W. Wang, Z. Qi, C. Zhao, H. Ji, Z. Zhang, Novel Raney-like nanoporous Pd catalyst with superior electrocatalytic activity towards ethanol electro-oxidation, *Int. J. Hydrogen Energy* 37 (2012) 2579–2587.
 - [22] C. Bianchini, P.K. Shen, Palladium-based electrocatalysts for alcohol oxidation in half cells and in direct alcohol fuel cells, *Chem. Rev.* 109 (2009) 4183–4206.
 - [23] S. Sun, Z. Jusys, R.J. Behm, Electrooxidation of ethanol on Pt-based and Pd-based catalysts in alkaline electrolyte under fuel cell relevant reaction and transport conditions, *J. Power Sources* 231 (2013) 122–133.
 - [24] E. Antolini, Palladium in fuel cell catalysis, *Energy Environ. Sci.* 2 (2009) 915–931.
 - [25] L. Ma, D. Chu, R. Chen, Comparison of ethanol electro-oxidation on Pt/C and Pd/C catalysts in alkaline media, *Int. J. Hydrogen Energy* 37 (2012) 11185–11194.
 - [26] Z.-Y. Zhou, Q. Wang, J.-L. Lin, N. Tian, S.-G. Sun, In situ FTIR spectroscopic studies of electrooxidation of ethanol on Pd electrode in alkaline media, *Electrochim. Acta* 55 (2010) 7995–7999.
 - [27] Y.-Y. Yang, J. Ren, Q.-X. Li, Z.-Y. Zhou, S.-G. Sun, W.-B. Cai, Electrocatalysis of ethanol on a Pd electrode in alkaline media: an in situ attenuated total reflection surface-enhanced infrared absorption spectroscopy study, *ACS Catal.* 4 (2014) 798–803.
 - [28] U. Martinez, A. Serov, M. Padilla, P. Atanassov, Mechanistic insight into oxide-promoted palladium catalysts for the electro-oxidation of ethanol, *ChemSusChem* 7 (2014) 2351–2357.
 - [29] B. Wu, N. Zheng, Surface and interface control of noble metal nanocrystals for catalytic and electrocatalytic applications, *Nano Today* 8 (2013) 168–197.
 - [30] J.W. Hong, D. Kim, Y.W. Lee, M. Kim, S.W. Kang, S.W. Han, Atomic-distribution-dependent electrocatalytic activity of Au–Pd bimetallic nanocrystals, *Angew. Chem.* 123 (2011) 9038–9042.
 - [31] S. Cheong, J.D. Watt, R.D. Tilley, Shape control of platinum and palladium nanoparticles for catalysis, *Nanoscale* 2 (2010) 2045–2053.
 - [32] Y. Xiong, Y. Xia, Shape-controlled synthesis of metal nanostructures: the case of palladium, *Adv. Mater.* 19 (2007) 3385–3391.
 - [33] Z. Bai, L. Yang, L. Li, J. Lv, K. Wang, J. Zhang, A facile preparation of hollow palladium nanosphere catalysts for direct formic acid fuel cell, *J. Phys. Chem. C* 113 (2009) 10568–10573.
 - [34] M. Jin, H. Zhang, Z. Xie, Y. Xia, Palladium concave nanocubes with high-index facets and their enhanced catalytic properties, *Angew. Chem. Int. Ed.* 50 (2011) 7850–7854.
 - [35] J.-S. Ye, C.-W. Chen, C.-L. Lee, Pd nanocube as non-enzymatic glucose sensor, *Sens. Actuators B: Chem.* 208 (2015) 569–574.
 - [36] Y. Wang, S.I. Choi, X. Zhao, S. Xie, H.C. Peng, M. Chi, C.Z. Huang, Y. Xia, Polyol synthesis of ultrathin Pd nanowires via attachment-based growth and their enhanced activity towards formic acid oxidation, *Adv. Funct. Mater.* 24 (2014) 131–139.
 - [37] H. Hu, Z. Jiao, J. Ye, G. Lu, Y. Bi, Highly efficient hydrogen production from alkaline aldehyde solutions facilitated by palladium nanotubes, *Nano Energy* 8 (2014) 103–109.
 - [38] X. Yin, X. Liu, Y.-T. Pan, K.A. Walsh, H. Yang, Hanoi tower-like multilayered ultrathin palladium nanosheets, *Nano Lett.* 14 (2014) 7188–7194.
 - [39] Y.-T. Pan, X. Yin, K.S. Kwok, H. Yang, Higher-order nanostructures of two-dimensional palladium nanosheets for fast hydrogen sensing, *Nano Lett.* 14 (2014) 5953–5959.
 - [40] X. Huang, S. Tang, X. Mu, Y. Dai, G. Chen, Z. Zhou, F. Ruan, Z. Yang, N. Zheng, Freestanding palladium nanosheets with plasmonic and catalytic properties, *Nat. Nanotechnol.* 6 (2010) 28.
 - [41] H.M. Rietveld, A profile refinement method for nuclear and magnetic structures, *J. Appl. Crystallogr.* 2 (1969) 65–71.
 - [42] J. Rodríguez Carvajal, Recent advances in magnetic-structure determination by neutron power diffraction, *Physica B* 192 (1993) 55–69.
 - [43] V. Germain, J. Li, D. Inger, Z.L. Wang, M.P. Pileni, Stacking faults in formation of silver nanodisks, *J. Phys. Chem. B* 107 (2003) 8717–8720.
 - [44] Y.H. Fang, Z.P. Liu, Electrochemical reactions at the electrode/solution interface: theory and applications to water electrolysis and oxygen reduction, *Sci. China Chem.* 53 (2010) 543–552.
 - [45] H. Bönemann, G. Khelashvili, Efficient fuel cell catalysts emerging from organo-metallic chemistry, *Appl. Organomet. Chem.* 24 (2010) 257–268.
 - [46] A. Zalineeva, S. Baranton, C. Coutanceau, G. Jerkiewicz, Electrochemical behavior of unsupported shaped palladium nanoparticles, *Langmuir* 31 (2015) 1605–1609.
 - [47] S. Henning, J. Herranz, H.A. Gasteiger, Bulk-palladium and palladium-on-gold electrocatalysts for the oxidation of hydrogen in alkaline electrolyte, *J. Electrochem. Soc.* 162 (2015) F178–F189.
 - [48] M. Lukaszewski, M. Soszko, A. Czerwiński, Electrochemical methods of real surface area determination of noble metal electrodes—an overview, *Int. J. Electrochem. Sci.* 11 (2016) 4442–4469.
 - [49] S. Trasatti, O.A. Petrii, Real surface area measurements in electrochemistry, *J. Electroanal. Chem.* 327 (1992) 353–376.
 - [50] K. Mohanraju, L. Cindrella, Impact of alloying and lattice strain on ORR activity of Pt and Pd based ternary alloys with Fe and Co for proton exchange membrane fuel cell applications, *RSC Adv.* 4 (2014) 11939–11947.
 - [51] J. Suntivich, H.A. Gasteiger, N. Yabuuchi, Y. Shao-Horn, Electrocatalytic measurement methodology of oxide catalysts using a thin-film rotating disk electrode, *J. Electrochem. Soc.* 157 (2010) B1263.
 - [52] S.J. Ye, D.Y. Kim, S.W. Kang, K.W. Choi, S.W. Han, O.O. Park, Synthesis of chestnut-like palladium nanostructures and their enhanced electrocatalytic activities for ethanol oxidation, *Nanoscale* 6 (2014) 4182–4187.
 - [53] J. Souza-Garcia, E. Herrero, J.M. Feliu, Breaking the C–C bond in the ethanol oxidation reaction on platinum electrodes: effect of steps and ruthenium adatoms, *ChemPhysChem* 11 (2010) 1391–1394.
 - [54] M. López-Atalaya, E. Morallón, F. Cases, J.L. Vázquez, J.M. Pérez, Electrochemical oxidation of ethanol on Pt(hkl) basal surfaces in NaOH and Na₂CO₃ media, *J. Power Sources* 52 (1994) 109–117.
 - [55] M. Shao, R.R. Adzic, Electrooxidation of ethanol on a Pt electrode in acid solutions: in situ ATR-SEIRAS study, *Electrochim. Acta* 50 (2005) 2415–2422.
 - [56] P.A. Christensen, S.W.M. Jones, A. Hamnett, In situ FTIR studies of ethanol oxidation at polycrystalline Pt in alkaline solution, *J. Phys. Chem. C* 116 (2012) 24681–24689.
 - [57] S.C.S. Lai, S.E.F. Kleijn, F.T.Z. Öztürk, V.C. van Rees Vellinga, J. Koning, P. Rodríguez, M.T.M. Koper, Effects of electrolyte pH and composition on the ethanol electro-oxidation reaction, *Catal. Today* 154 (2010) 92–104.
 - [58] Z.Y. Zhou, Q. Wang, J.L. Lin, N. Tian, S.G. Sun, In situ FTIR spectroscopic studies of electrooxidation of ethanol on Pd electrode in alkaline media, *Electrochim. Acta* 55 (2010) 7995–7999.
 - [59] P.A. Christensen, A. Hamnett, D. Linares-Moya, The electro-oxidation of formate ions at a polycrystalline Pt electrode in alkaline solution: an in situ FTIR study, *Phys. Chem. Chem. Phys.* 13 (2011) 11739–11747.
 - [60] M. Figueiredo, R. Arán Ais, V. Climent, T. Kallio, J. Feliu, Evidence of local pH changes during ethanol oxidation at Pt electrodes in alkaline media, *ChemElectroChem* 2 (2015) 1254–1258.
 - [61] E.A. Monyoncho, S.N. Steinmann, C. Michel, E.A. Baranova, T.K. Woo, P. Sautet, Ethanol electro-oxidation on palladium revisited using polarization modulation infrared reflection absorption spectroscopy (PM-IRRAS) and density functional theory (DFT): why is it difficult to break the C–C bond? *ACS Catal.* 6 (2016) 4894–4906.
 - [62] X. Fang, L. Wang, P.K. Shen, G. Cui, C. Bianchini, An in situ Fourier transform infrared spectroelectrochemical study on ethanol electrooxidation on Pd in alkaline solution, *J. Power Sources* 195 (2010) 1375–1378.
 - [63] R.B. Kutz, B. Braunschweig, P. Mukherjee, D.D. Dlott, A. Wieckowski, Study of ethanol electrooxidation in alkaline electrolytes with isotope labels and sum-frequency generation, *J. Phys. Chem. Lett.* 2 (2011) 2236–2240.
 - [64] J.S. Spendlow, J.D. Goodpaster, P.J.A. Kenis, A. Wieckowski, Mechanism of CO oxidation on Pt(111) in alkaline media, *J. Phys. Chem. B* 110 (2006) 9545–9555.
 - [65] J.S. Spendlow, G.Q. Lu, P.J.A. Kenis, A. Wieckowski, Electrooxidation of adsorbed CO on Pt(111) and Pt(111)/Ru in alkaline media and comparison with results from acidic media, *J. Electroanal. Chem.* 568 (2004) 215–224.
 - [66] P.P. Lopes, D. Strmcnik, J.S. Jirkovsky, J.G. Connell, V. Stamenkovic, N. Markovic, Double layer effects in electrocatalysis: the oxygen reduction reaction and ethanol oxidation reaction on Au(111), Pt(111) and Ir(111) in alkaline media containing Na and Li cations, *Catal. Today* 262 (2016) 41–47.
 - [67] J.L. Rodríguez, E. Pastor, X.H. Xia, T. Iwasita, Reaction intermediates of acet-aldehyde oxidation on Pt(111) and Pt(100). An in situ FTIR study, *Langmuir* 16 (2000) 5479–5486.
 - [68] R.B. Kutz, B. Braunschweig, P. Mukherjee, R.L. Behrens, D.D. Dlott, A. Wieckowski, Reaction pathways of ethanol electrooxidation on polycrystalline platinum catalysts in acidic electrolytes, *J. Catal.* 278 (2011) 181–188.